VOLCΛNICΛ

Widespread phosphorous excess in olivine, rapid crystal growth, and implications for magma dynamics

● Cin-Ty A. Lee*[α], ● Chenguang Sun[β], Eytan Sharton-Bierig[α], Patrick Phelps[α], Jackson Borchardt[α], Boda Liu[α,γ], ● Gelu Costin[α], and A. Dana Johnston[δ]

[α] Department of Earth, Environmental and Planetary Sciences, 6100 Main St., Rice University, Houston, TX 77005, USA.
[β] Department of Geological Sciences, Jackson School of Geosciences, University of Texas, Austin, TX 78705, USA.
[γ] State Key Laboratory of Lithospheric Evolution, Institute of Geology and Geophysics, Chinese Academy of Sciences, Beijing 100029, China.
[δ] Department of Earth Sciences, 1272 University of Oregon, Eugene, OR 97403, USA.

ABSTRACT

Trace element zoning is often used to unravel the crystallization history of phenocrysts in magmatic systems, but interpretation requires quantifying the relative importance of equilibrium versus disequilibrium. Published partition coefficients for phosphorous (P) in olivine vary by more than a factor of ten. After considering kinetic effects, a new equilibrium partition coefficient was extrapolated from a re-examination of natural and experimental systems, indicating that P partition coefficients in olivine are significantly over-estimated. These new partitioning constraints allow us to establish a theoretical P Equilibrium Fractionation Array (PEFA) for mid-ocean ridge basalts (MORBs), revealing that most olivines from MORBs have excess P (2–15 times PEFA) and are thus in disequilibrium. Using an independent case study of natural dendritic olivines, we show that such P enrichments can be explained by diffusion-limited incorporation of P during rapid crystal growth. If growth rate can be related to cooling, the rapid growth rates of olivines have implications for magma system dynamics, such as the size of magma bodies or where crystallization occurs within the body.

KEYWORDS: Olivine; Dendrites; Magma chamber; Crystallization; Crystal growth; Phosphorous.

1 INTRODUCTION

Volcanism is a distinctive feature of dynamic rocky planets, such as the Earth. Although most of the Earth's mantle is solid, small amounts of partial melt or magmas are generated where the mantle upwells. These magmas depart the mantle and ascend to the Earth's surface, generating the crust beneath the ocean basins and the building blocks of continental crust. However, by the time these melts complete their journey to the surface, they no longer resemble their parental compositions. Instead of rising immediately to the surface, they more typically ascend in stages or steps, during which they cool and partially crystallize, and ensuing gravitational segregation of crystals causes the composition of the remaining magma to evolve [Edmonds et al. 2019]. Magmas can also undergo crystal accumulation, assimilation of pre-existing crust, and mixing with other magmas during this protracted journey [De-Paolo 1981; Hildreth and Moorbath 1988; Lee and Chin 2014]. Collectively, these processes give rise to the compositional diversity of Earth's magmas and crust.

There are many questions related to how magmas journey from the mantle to the surface. When and where do magmas stage in the crust, and how many staging points are there? How large are magma bodies at each staging point? Are large magmatic bodies assembled over long time periods from small magma bodies? How long do magma bodies stay molten in the crust? Are these staging reservoirs replenished, how much crystal segregation occurs, and do the magmatic bodies interact with each other? Geochemical methods are often invoked to address some of these questions. A common approach is to use chemically zoned crystals to reconstruct the history of these magmas, the premise being that any physical changes of a magma body are reflected in changes in its composition and that the compositions of crystals faithfully record such changes (Figure 1A). However, the incorporation of elements into a crystal may sometimes be controlled by kinetic processes and thus may not represent the composition of the overall magma body (Figure 1B) [Bacon 1989; Watson and Müller 2009; Welsch et al. 2014; Sossi and O'Neill 2016; Baziotis et al. 2017; 2019; Shea et al. 2019].

Here, we explore how trace elements are incorporated into growing crystals. We focus specifically on trace element incorporation into olivine, a common phenocryst mineral in basaltic magmas. We then develop a framework for quantifying trace element disequilibria, which we, in turn, use to constrain crystal growth rate with implications for the thermal history of magma bodies.

2 BASIC CONCEPTS OF TRACE-ELEMENT INCORPORATION DURING RAPID CRYSTAL GROWTH

At equilibrium, the concentration of a trace element in a crystal is controlled by the equilibrium partition coefficient between the crystal and the melt or fluid. This partition coefficient reflects the state in which chemical potential of the element in the crystal and the fluid are equal so that there are no gradients driving elemental exchange. Such a condition further implies that the melt/fluid is homogeneous and the composition of the crystal reflects both near and far-field composition of the melt/fluid.
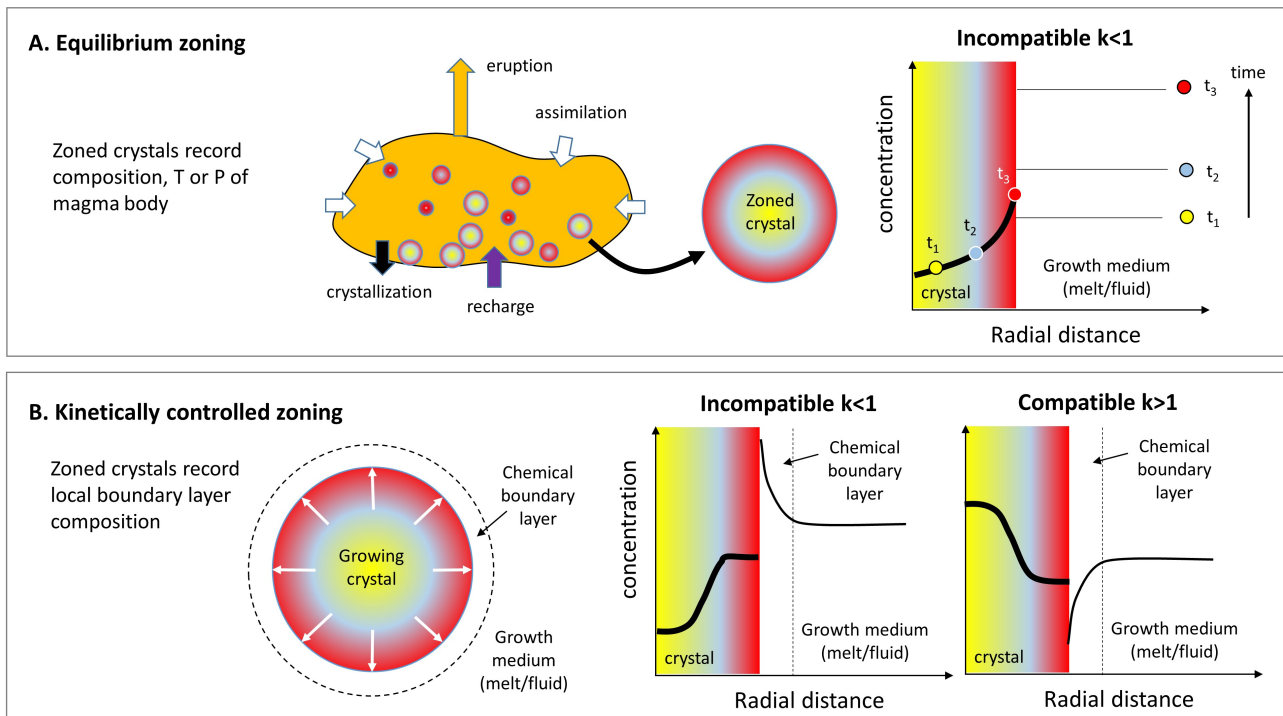
*✉ ctlee@rice.edu

Figure 1: [A] Equilibrium mineral zoning wherein zoning reflects changes in temperature, pressure, or the far-field magma composition due to fractional crystallization, recharge or mixing. Cartoon magma chamber and zoomed in schematic of a zoned crystal are shown. Right hand plot shows concentration versus radial distance in a crystal for an incompatible element ($k < 1$). Left side of plot represents the crystal. Right side represents the melt. Melt is assumed to be well-mixed so melt compositions are spatially constant. Melt composition at different times, t_1, t_2, and t_3 are shown. Changes in melt composition with time are reflected as zoning within the phenocryst. [B] Kinetically limited mineral zoning wherein zoning reflects only the composition of the local boundary layer in the melt, not the far-field melt composition. This is due to rapid growth compared to diffusive transport of a trace element in the melt. Right hand plots show concentration versus radial distance for incompatible ($k < 1$) and compatible ($k > 1$) elements. Left hand side of each plot represents the crystal. Right hand side represents the melt. For incompatible elements, an enriched boundary layer in the melt develops. The phenocryst begins in equilibrium with the far-field melt composition, but eventually becomes enriched on the rim as the boundary layer develops. For compatible elements, the phenocrysts evolve to being depleted while the melt becomes enriched. Note that in both cases, steady state can eventually be attained. Melt concentration profile represents steady state. Zonation in phenocryst records evolution from initial state to steady state, where radius qualitatively represents time.

In practice, equilibrium conditions may not be attained. In fact, crystal nucleation and growth are ultimately driven by supersaturation, so disequilibrium may be the norm when crystals are growing. If a trace element in the melt/fluid cannot be delivered quickly enough to the growing crystal, such as in the case of a slowly diffusing element (i.e. where rate of diffusion of the trace element is slower than the rate of crystal growth), a concentration gradient may develop in the melt/fluid and the crystal is then only in near-field equilibrium with the melt/fluid [Watkins et al. 2017]. This scenario is referred to as transport-limited kinetics. Another disequilibrium scenario, referred to as attachment kinetics, occurs when rapid crystal growth modifies how atoms of the trace element are attached to the growing crystal surface. Rapid crystal growth can result in imperfections in the crystal lattice (e.g. vacancies, impurities, etc.) that influence how atoms are incorporated, resulting in an effective partition coefficient that deviates from that of equilibrium [Watkins et al. 2017]. While we do not know which process dominates, transport-limited

kinetics are common in magmatic systems and especially in olivine, so here we focus on that scenario.

In a transport-limited regime, the concentration of a trace element in the melt ahead of a growing crystal front represents a balance between the rate at which the element is consumed (compatible) or rejected (incompatible) by the growing crystal and the rate at which the element in the liquid can homogenize with the far-field melt. If trace element transport rates (high diffusivity or high advection rates) in the melt are high relative to crystal growth rates, the growing crystal surface maintains equilibrium with the far-field melt. However, if crystal growth rates are fast compared to trace element transport rates in the melt, a steady state chemical boundary layer develops ahead of the growing crystal front because incompatible elements build up and compatible elements become depleted in the boundary layer (Figure 1B). Because the crystal equilibrates with the local boundary layer, not with the far-field melt, concentrations in the crystal deviate strongly from far-field equilibrium [Watson 1996; Sunagawa 2010].

At steady state, the relative enrichment/depletion of a trace element in the liquid boundary layer or growing crystal is given by Burton et al. [1953]

$$\frac{C_\mathrm{x}}{C_\mathrm{xeq}} = \frac{C_\mathrm{Lo}}{C_\mathrm{Leq}} = \frac{k_\mathrm{eff}}{k_\mathrm{o}} = \frac{1}{k_\mathrm{o} + (1 - k_\mathrm{o})exp(-V\delta/D)} \quad (1)$$

where C_Lo is the concentration of the element in the liquid at the crystal-liquid interface (μg/g), C_x is the concentration on the crystal rim, C_Leq is the concentration of the liquid far away from the crystal, C_xeq is the concentration in the crystal if it were in equilibrium with the far-field liquid, D is chemical diffusivity (m^2/s) in the melt, V is the crystal growth rate (m/s), δ is the width of the chemical boundary layer (m), k_o is the equilibrium partition coefficient between the crystal and melt ($k_\mathrm{o} = C_\mathrm{x}/C_\mathrm{Lo} = C_\mathrm{xeq}/C_\mathrm{Leq}$), and k_eff is the effective apparent partition coefficient of the crystal relative to the far-field liquid ($k_\mathrm{eff} = C_\mathrm{x}/C_\mathrm{Leq}$). For most of the elements of interest, solid state diffusion within the crystal is assumed to be negligible on the timescales of crystal growth. Equation 1 is a measure of the extent to which the crystal composition deviates from equilibrium with the far-field melt and is widely used in the material science community to describe crystallization in both static and dynamic systems [Burton et al. 1953; Sunagawa 2010]. The quantity $V\delta/D$ is a Peclet number that represents a measure of crystal growth rate relative to chemical diffusion rates. At high Peclet number, when crystal growth rate outpaces chemical diffusion, disequilibrium is maximized such that $C_\mathrm{x}/C_\mathrm{xeq} = C_\mathrm{L}/C_\mathrm{Leq} = 1/k_\mathrm{o}$, that is, $k_\mathrm{eff} = 1$ and the crystal's trace element concentration is identical to that of the melt for both incompatible and compatible trace elements (there is of course a correction if the molecular weight of the crystal and melt are not the same). In contrast, at low Peclet number, when diffusive re-equilibration in the melt is rapid compared to crystal growth, the system approaches far-field equilibrium, $C_\mathrm{x}/C_\mathrm{xeq} = C_\mathrm{L}/C_\mathrm{Leq} = 1$, and no kinetic enrichments or depletions in trace elements develop.

3 EXTREME PHOSPHOROUS DISEQUILIBRIUM IN RAPIDLY GROWN DENDRITIC OLIVINE

To test these concepts, we investigated olivine crystals, which based on their crystal morphologies, grew rapidly. We chose a unique occurrence of dendritic olivine crystals from an alkali mafic plug on the island of Kaua'i in the Hawaiian Island chain [Johnston and Stout 1984a; Johnston et al. 1985]. The plug, measuring approximately 200 m in diameter, intruded Pleistocene Koloa volcanic series and likely represents a remnant feeder pipe to post-erosional alkalic lavas, which have since been eroded [Johnston et al. 1985]. The plug consists of a highly oxidized margin. The plug's margin consists of olivine-rich peridotite xenoliths supported by a quenched alkali basalt melt matrix. Oxybarometry from previous studies indicates that crystallization of the matrix melt occurred under oxygen fugacities 10^6 times more oxidizing than that of the mantle, approaching that of the atmosphere, and suggesting that crystallization occurred at near-surface conditions, perhaps even with direct interaction with the atmosphere [John-

ston and Stout 1984a; b; Johnston et al. 1985; Johnston and Beckett 1986].

These unusually oxidizing conditions imparted unique characteristics to the system. The xenoliths are mantled by 5 mm thick dark rinds composed of micron scale symplectic intergrowths of Fe^{3+}-oxide (ferrite) and orthopyroxene crystals within the olivine rims (Figure 2A) [Johnston and Stout 1984b]. This feature is the result of oxidation, wherein oxidation of Fe^{2+} dissolved in the olivine structure causes exsolution of discrete intergrowths of Fe^{3+}-bearing oxides (ferrite) and orthopyroxene, leaving behind olivines that are substantially more magnesian (forsteritic) than olivine in the xenolith cores (Figure 2). Forsterite (Fo) contents (atomic Mg/(Mg+Fe)×100) increase from normal values of 88–90 in the xenolith interiors to values in excess of 96. Oxidation also affected the matrix melt, which consists of subhedral to acicular clinopyroxene, feldspar and olivine crystals. Canary-yellow clinopyroxene crystals are rich in acmite (NaFe^{3+}) and olivine crystals have forsterite contents approaching 98, representing some of the highest forsterite contents ever recorded for magmatic olivines on Earth [Johnston and Stout 1984a]. Some dendritic olivines show distinct "swallowtail" or needle-like shapes (Figure 2A and B). In these, forsterite content increases towards the dendrite tips. Collectively, these observations indicate that crystal growth and oxidation of the system occurred simultaneously, with forsterite content being a qualitative measure of crystallization time or reaction progress.

We can estimate the timescales of crystallization from the thickness of the oxidation rinds on the xenoliths (Figure 2A). Such oxidation is likely controlled by H diffusion rather than by direct diffusion of O$_2$ [Kohlstedt and Mackwell 1998; Demouchy and Mackwell 2006]. At the temperatures typical of the host magma (~1200 °C), H diffusivity associated with redox exchange in olivine is ~10^{-9} m^2/s [Kohlstedt and Mackwell 1998; Demouchy and Mackwell 2006]. Taking the 5 mm thick oxidation rind of the xenoliths as a measure of the characteristic diffusion distance, we find a characteristic time for oxidation of ~1–3 hours with the following scaling $t \sim x^2/(4D_H)$, where x is the rind thickness and D_H is diffusivity. For the swallow-tailed dendritic olivines, which are ~5 mm in length and <50 μm in width, this corresponds to a growth rate of ~1–3 mm/h. These growth rates approach those in pegmatitic systems [Phelps et al. 2020] and are consistent with the presence of dendritic olivines [Faure 2006].

We now turn to the trace element geochemistry of the olivines (Supplementary Table 1). Xenolith olivines are characterized by high Ni, which is compatible in olivine, and low Ca, Al, P, Ti, Mn and Na, which are incompatible in olivine. By contrast, olivine in the magmas are enriched in Ca, Al, P, Ti, Mn and Na but highly depleted in Ni. P, Al, Ti and Na contents are some of the highest ever measured in terrestrial olivines, with P$_2$O$_5$ contents exceeding 1 wt. % (Figure 3A). Positive correlation of P with Na and negative correlation of P with Si suggests that P is incorporated into the Si site and charge balanced by Na. P, Al, Ti and Na enrichments increase towards olivine rims, especially towards the tips of dendritic olivines (Figure 3). We also note that apatite, a phosphate mineral, preferentially nucleates within 50 μm of the swal-
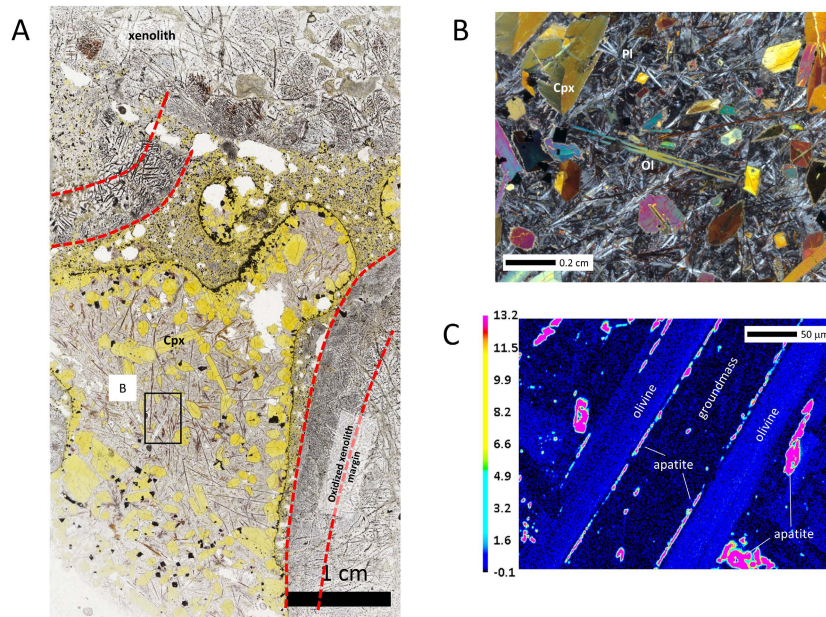
Figure 2: Case study of dendritic olivine from Kaua'i, Hawai'i. [A] Plane transmitted light image of cumulate peridotite xenolith (top half and lower right) encased in host alkali basalt (lower left corner). Xenolith consists of olivine grains from which Fe^{3+}-oxides (ferrite) have exsolved (black minerals). Oxidized margins of xenolith show more exsolution of ferrite and appear darker. Host lava consists of olivine, clinopyroxene (Cpx) and feldspar matrix along with elongated crystals of clinopyroxene (light yellow colors). Rectangle labeled "B" represents zoomed in area in B. [B] Close up of lava groundmass in crossed polarized transmitted light (see rectangle in A). Long, swallow-tailed grain in center is a dendritic olivine (Ol) that was analyzed in detail in this study. Cpx = clinopyroxene. [C] Electron probe micro-analysis WDS map of P for the dendritic olivine in B. Dendritic olivine is blue. Red areas represent apatite, a P-bearing accessory phase. Tip of olivine dendrite needle is towards the lower left. Scale bar represents P_2O_5 in wt. %.
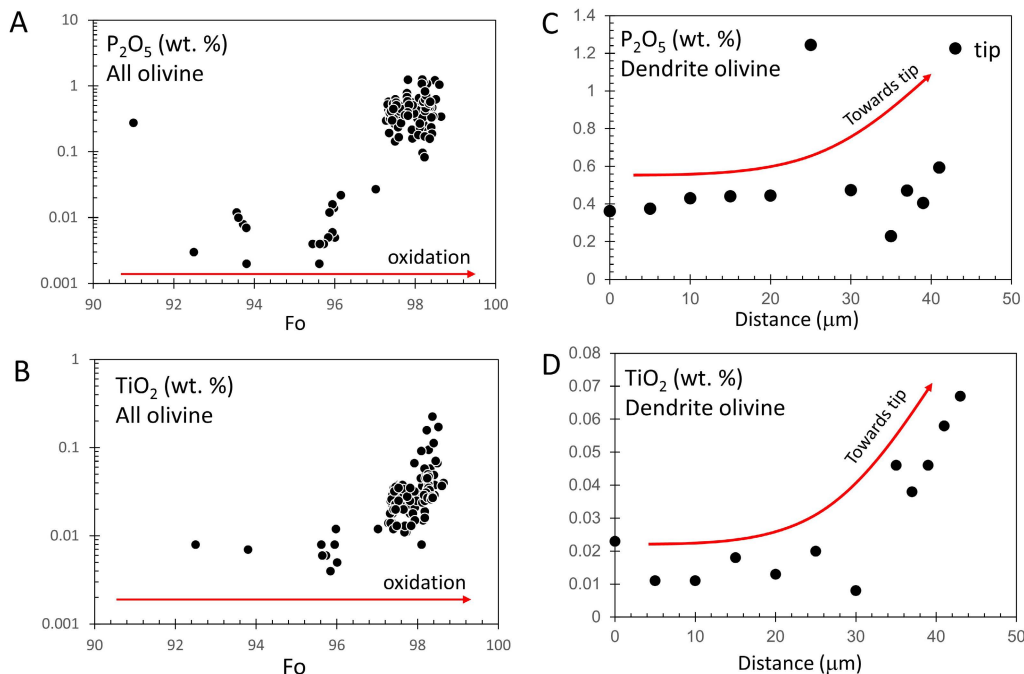
Figure 3: Case study of dendritic olivine from Kaua'i, Hawai'i. [A] and [B] P_2O_5 and TiO_2 versus Fo (atomic Mg/(Mg+Fe)×100) in olivines. Data pertain to olivines from peridotite xenoliths and olivine phenocrysts within the host lava, including the swallowtail-shaped dendritic olivine in Figure 2B. [C] P_2O_5 in wt. % along the long-axis of one olivine dendrite blade in Figure 2B and C. Tip of dendrite blade is on the right. [D] TiO_2 in wt. % for the same dendrite blade as in [C]. Both P_2O_5 and TiO_2 increase towards the tip of the olivine blades.

lowtail olivines (Figure 2C). Qualitatively, these observations are consistent with rapid olivine growth, which generates a P-enriched boundary layer in the melt because P, being incompatible, is preferentially rejected from olivine. As P increases in the boundary layer, the growing olivine crystal begins to inherit the high P of the melt. P in the enriched melt boundary layer eventually reaches concentrations high enough to saturate apatite. The nucleation of apatite in these boundary layers has previously been observed during plagioclase crystallization and interpreted similarly [Bacon 1989]. Our conclusions are consistent with the results of Boesenberg and Hewins [2010], who showed experimentally that rapidly crystallized olivine can incorporate P in excess of 1 wt. %. Although not to the extreme levels seen here, enrichments in olivine of P and other trace elements have previously been reported in olivine phenocrysts, olivine cumulates and mantle xenoliths. Disequilibrium associated with rapid crystal growth has been qualitatively invoked to explain such enrichments [Milman-Barris et al. 2008; Mallmann et al. 2009; Welsch et al. 2012; Baziotis et al. 2017; 2019; Shea et al. 2019; Wieser et al. 2020].

To quantify the extent of disequilibria in the olivine crystals, we divide matrix olivine's trace element concentrations by that in olivines from the peridotite xenolith cores. Because of their low incompatible element and high compatible element concentrations, we take the xenolith olivines to represent our best approximation of equilibrium with the far-field melt (we recognize that the xenolith olivines themselves may not have equilibrium trace element contents, so this approach places a minimum bound on the extent of disequilibrium in the olivine crystals). From Figure 4A, it can be seen that incompatible elements are all enriched relative to equilibrium, while the only compatible element measured—Ni—is depleted. When plotted against the element's diffusivity in a melt (where we have assumed a temperature of 1200 °C), we find that the disequilibrium enrichment of incompatible trace elements correlates negatively with diffusivity, such that slowly diffusing incompatibles are enriched more than rapidly diffusing elements (diffusion parameters for Ni, Ca, Mn, P, Al and Ti taken from the literature (Figure 4A) [Lowry et al. 1982; Chen and Zhang 2008; Behrens and Hahn 2009; Zhang et al. 2010; Watson et al. 2015]. These patterns are consistent with the influence of crystal growth on trace element incorporation. In particular, for a boundary layer thickness δ of ~50 μm and a crystal growth rate of 1 mm/h, as noted above, it can be seen that the array displayed by incompatible elements fall on a crystal growth curve corresponding to a partition coefficient k_o of ~0.01, with slow diffusing elements like Al and P reaching the maximum enrichment of $1/k_o = 100$ (Figure 4). These results are consistent with the buildup of incompatible elements along a boundary layer next to the growing crystal due to rapid crystal growth and slow diffusion in the melt [Watson 1996; Milman-Barris et al. 2008; Welsch et al. 2012].

We note that a recent experimental study showed decoupling of P and Al enrichments in rapidly grown olivines [Shea et al. 2019]. In particular, a P-enriched boundary layer in the melt was not observed, leading the authors to conclude that P is controlled by growth-rate dependent attachment kinetics (resulting in disequilibrium partitioning) rather than by dif-

fusion kinetics in the melt [Shea et al. 2019]. Although we cannot measure the melt in this study directly because it has crystallized, P, Al and Ti are all enriched towards the tip of the olivine dendrites, suggesting they are controlled by similar kinetic processes. The fact that we see apatite along the edge of the olivine dendrites also supports the generation of a P-rich boundary layer during rapid growth and slow diffusion. More work is of course necessary to explore whether growth-rate dependent partitioning can also explain our observations.

4   Equilibrium partition coefficients for phosphorous revisited

Here, we further evaluate the robustness of our transport-limited models by comparing model-predicted k_o to actual k_o. Ni depletion is matched by the curve for $k_o = 10$, which is consistent with experimental constraints (Figure 4A). However, large uncertainties persist for the incompatible elements. For example, published P partition coefficients for olivine vary from 0.01 to nearly 1, with most values centered around 0.1 (Figure 5A) [Anderson and Greenland 1969; Ulmer 1989; Libourel 1994; Toplis et al. 1994; Brunet and Chazot 2001; Adam and Green 2006; Foley et al. 2010; Grant and Kohn 2013]. This high variability in published P partition coefficients is thus of limited use in evaluating the robustness of our models. Partitioning data for Al, Ti and Na in olivine are equally uncertain or non-existent due to analytical challenges of measuring their normally low abundances in olivine. Experimental studies are also faced with the possibility of disequilibrium if crystal growth outpaces diffusive transport in the melt [Boesenberg and Hewins 2010; Grant and Kohn 2013].

Appropriate natural systems can be used to infer equilibrium partition coefficients of highly incompatible elements. For example, the bulk partition coefficient of P between the peridotitic mantle and basaltic melt can be determined by bootstrapping to other elements for which partitioning behavior is known [Hofmann 1988]. In mid-ocean ridge basalts (MORBs), we find that P correlates best with Pr, so P bulk partitioning during mantle melting should be like that of Pr (Figure 5B). This correlation is purely coincidental and not causal because the crystal chemistry of P and Pr substitution into silicate minerals are obviously different. However, for the present purposes of placing bounds on P bulk partitioning, the mechanisms are not important. Workman and Hart [2005] used abyssal peridotites and modeling to infer a Pr bulk partition coefficient of 0.027. In a previous study from our lab, we showed that P contents in depleted mantle peridotites are similar between clinopyroxene, orthopyroxene and olivine [He et al. 2019], so if the bulk Pr partition coefficient can be translated to a bulk P partition coefficient, the P olivine/melt partition coefficient must be 10 times lower than most values published in the literature (~0.01).

We can also gain insight on partitioning from phenocryst-glass pairs. To do this, we studied olivine-rich MORB glasses from Siqueiros MORB glass from the East Pacific Rise (Supplementary Tables 2 and 3). Apparent partition coefficients were determined by dividing the measured P in olivine rims by the measured P content of the glass immediately adjacent to the olivine (Figure 5A). These apparent partition coefficients
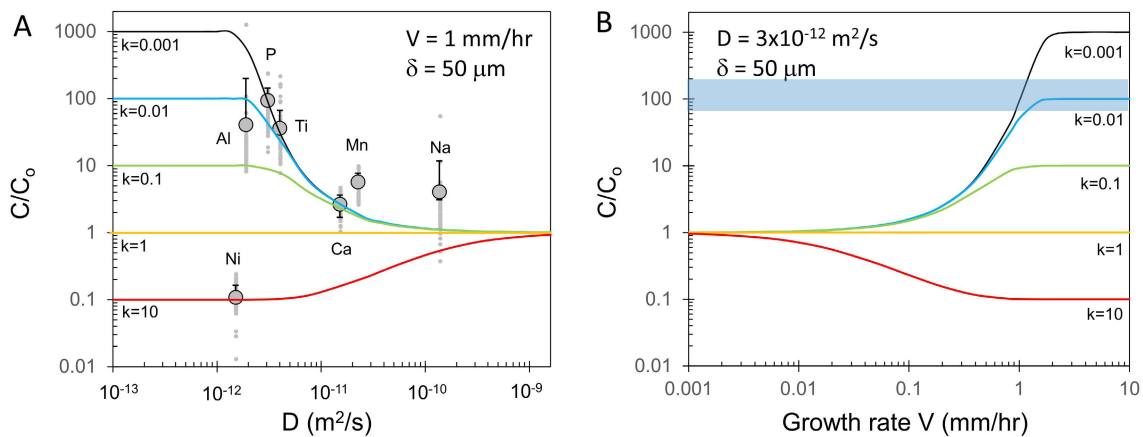
Figure 4: Models of trace-element incorporation during rapid crystal growth. [A] Vertical axis represents enrichment or depletion of element in swallowtail olivine relative to equilibrium conditions by normalizing concentrations in the swallowtail olivine (C) to concentrations in olivines from cumulate peridotite xenoliths (C_o). Enrichment/depletion factors (C/C_o) in olivine plotted against diffusivity in basaltic melt at 1200 °C using diffusion parameters from the literature [Lowry et al. 1982; Chen and Zhang 2008; Behrens and Hahn 2009; Zhang et al. 2010; Watson et al. 2015]. Curves represent steady state enrichment/depletion during rapid crystal growth. A crystal growth rate of 1 mm/h was estimated from the length scales of the oxidized xenolith rinds (see text). A boundary layer δ of 50 μm was assumed based on elemental maps (see text and Figure 1C). Different colored lines correspond to different mineral/melt equilibrium partition coefficients k. Compatible elements ($k > 1$) become depleted in growing crystal while incompatible elements ($k < 1$) become enriched. [B] Models of enrichment/depletion within olivine versus crystal growth rate for a diffusivity of 3×10^{-12} m²/s in the melt. This diffusivity corresponds with the diffusivity of P in basaltic melt at 1200 °C. Boundary layer thickness as in [C].
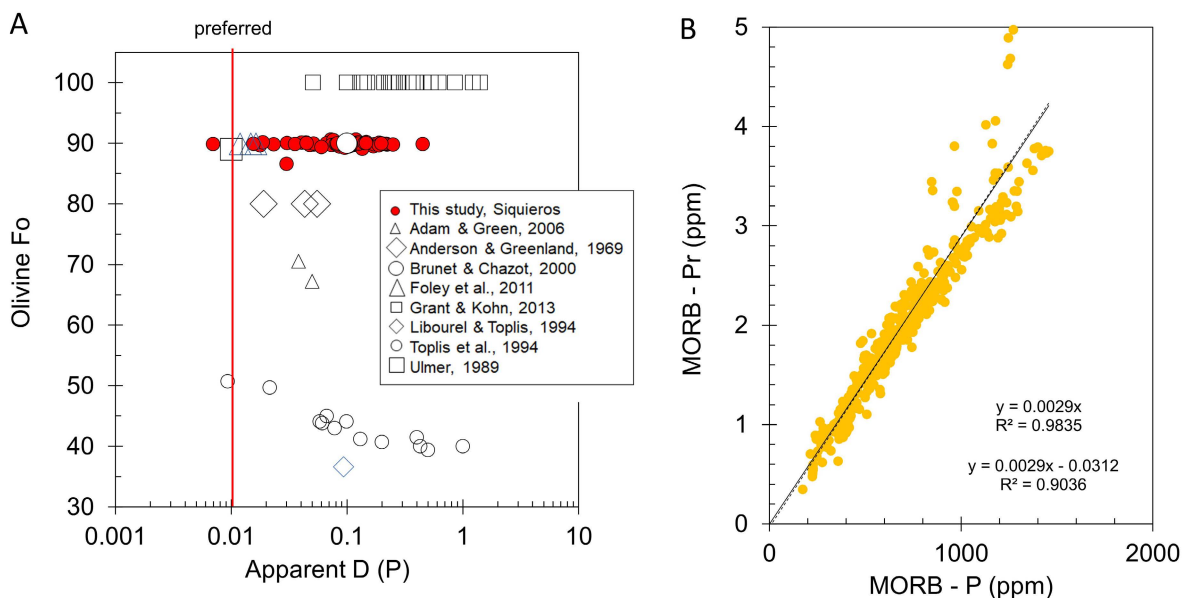
Figure 5: Constraints on P partitioning in olivine. [A] Apparent olivine/melt partition coefficients from Siqueiros MORB (this study), where natural olivine P content in olivine is divided by glass P content (red symbols). All other symbols represent estimates of olivine/melt partitioning from experiments or natural phenocryst/magma pairs. Data sources in legend and text. Vertical red line denotes preferred olivine/melt partition coefficient (see text). References for partition coefficients from the literature are in the text. [B] P (ppm by metal) versus Pr (ppm by metal) in mid-ocean ridge basalt (MORB) glass [Jenner and O'Neill 2012]. Data were linearly regressed. Regression parameters for a regression forced and unforced through the origin are shown. The fact that the regression is indistinguishable from one that is forced through the origin indicates that bulk partitioning of P during mantle melting is identical to that of Pr.

vary by more than a factor of 10, even though our Siqueiros olivines come from just two hand samples. The large variation in apparent partition coefficients is caused not by variability in the glass composition but in olivine compositions, suggest-

ing that many of the olivines are in disequilibrium in terms of P. Disequilibrium should lead to anomalously high P contents [Boesenberg and Hewins 2010; Grant and Kohn 2013], so the lowest apparent partition coefficients in our study and the literature (~0.01) must be closest to equilibrium. We thus take ~0.01 as our preferred estimate of the olivine/melt partition coefficient during mantle melting. Referring to Figure 4A, it can be seen that crystal growth models for a P partition coefficient of ~0.01 match our observed P enrichments in the swallowtail olivines from Kauaʻi, indicating that the crystal growth model adopted here may be applicable.

We recognize that the above results and discussions, while consistent with transport-limited kinetics, do not prove that transport-limited kinetics control the observed disequilibria. There are many assumptions (constant growth rate) and uncertainties (boundary layer thickness, diffusivities, equilibrium partition coefficients). We also recognize that the above analyses do not rule out the possibility for attachment kinetics being important or even dominant. Indeed, growth-rate dependent partitioning has been suggested for P [Shea et al. 2019], but whether such a process can explain the disequilibria we see in multiple trace elements is unclear. More work is necessary to resolve these questions, but given that transport-limited models can explain much of the observed disequilibria in this study, we explore now the implications of our observations in the context of transport-limited kinetics.

5 Widespread deviation of olivine crystals from the Phosphorous Equilibrium Fractionation Array (PEFA)

Motivated by the above proof-of-concept study, we extended our study to a survey of olivines from different magmatic environments (Supplementary Tables 4 and 5). We focused only on P for this study because data for other incompatible elements in olivine are too sparse. Even for P, the detection limits are too high in many historical studies to be useful. We compiled and measured high quality P content in olivines where detection limits were <0.001 wt. % P_2O_5. P_2O_5 contents of arc magmas, komatiites, and oceanic intraplate magmas (Hawaiʻi, Iceland, and Canary Islands) are shown in Figure 6. There are unfortunately few MORB olivine datasets of sufficient P data quality, so the Siquieros olivine data measured in this study are the only measured MORB olivines presented (Figure 6A). We avoid continental intraplate magmas because these magmas can be intrinsically rich in P and would introduce an additional variable into the P systematics of olivines.

As shown above, quantifying disequilibrium enrichment of P first requires an equilibrium reference. To establish this reference, we calculated the olivine composition that would hypothetically be in equilibrium with MORB, using a global dataset of MORB glasses from Jenner and O'Neill [2012]. Hypothetical equilibrium olivine forsterite content was calculated assuming an equilibrium Fe/Mg exchange coefficient (K_D = $(Fe/Mg)^{olivine}/(Fe/Mg)^{melt}$) of 0.32, which is relatively independent of temperature (no correction was made for Fe^{3+} in the melt as this effect is insignificant on the scale of compositional variation observed in MORBs) [Roeder and Emslie

1970; Tamura et al. 2000]. Hypothetical equilibrium P content of olivine was calculated by dividing MORB glass P content by the P equilibrium partition coefficient k_P. For primitive mantle derived melts, which form by melting at temperatures of ~1300 °C [Lee et al. 2009], we used a partition coefficient of 0.01 as derived above. More evolved magmas have cooled and differentiated from their primary compositions, so a correction to lower temperatures is needed to calculate the hypothetical equilibrium P content of olivines with lower forsterite content. Temperatures of MORB glass were estimated from glass MgO content [Lee and Chin 2014]. For a given temperature, k_P can be calculated using an Arrhenius relationship, but published partitioning data for P are too scattered to estimate P activation energy directly. Instead, we inferred the P activation energy from Ti partitioning assuming that Ti and P both substitute in the Si site as evidenced by positive correlations of Ti with P and negative correlations of Ti and P with Si in the Hawaiian swallowtail olivines (this study) and in olivine partitioning experiments [Mallmann et al. 2009]. We used the experimental data of Grove and Juster [1989] and Toplis and Carroll [1996] to arrive at an empirical linear relationship between $\ln(D_{Ti})$, $1/T$ (in degrees Kelvin; K) and wt. % Al_2O_3 in olivine, the latter to account for the small effect of olivine or magma composition ($\ln(D_{Ti}) = 20.2 + 22980(1/T(K) + 4.6\ Al_2O_3$), yielding an activation energy of 191 kJ/mol for D_{Ti}. To convert the Ti activation energy to that of P, we applied an empirical linear regression between $\ln(D_{Ti})$ and $\ln(D_P)$ using the olivine/melt partitioning experiments of [Mallmann et al. 2009]. After correction, this yields an activation energy of 352 kJ/mol for D_P in olivine.

The above approach was used to calculate hypothetical equilibrium olivine compositions for MORBs, defining a trend of decreasing P_2O_5 with increasing forsterite (Figure 6A). To extend the range of equilibrium olivine to higher forsterite contents, we measured the P contents of olivines in oceanic mantle as sampled by residual peridotite xenoliths from volcanoes on the oceanic islands of Samoa [He et al. 2019]. Our rationale for choosing oceanic mantle peridotites is that they partially melted at great depths, high temperatures, and on timescales long enough that the approach to equilibrium is more likely than for phenocrysts. In addition, unlike continental mantle, oceanic mantle tends to be less disturbed by subsequent metasomatic processes that could introduce P into the system. In Figure 6A, we can see that the Samoan oceanic mantle olivines extend the equilibrium MORB olivine array to higher forsterite and lower P contents, lending confidence that the MORB olivine array is a meaningful estimate of equilibrium P contents. The increase in olivine P with decreasing Fo represents the effect of fractional crystallization on increasing the P content of the differentiating magma because P is incompatible in all crystallizing phases until the system reaches apatite saturation. This negative correlation should be broadly universal, but the exact relationship should of course depend on how melt Mg# (atomic Mg/(Mg+Fe) × 100) and olivine forsterite (Fo) vary with residual melt fraction for different petrogenetic histories.

Here, we combine calculated equilibrium MORB olivine and measured oceanic mantle to define an empirical equilib-
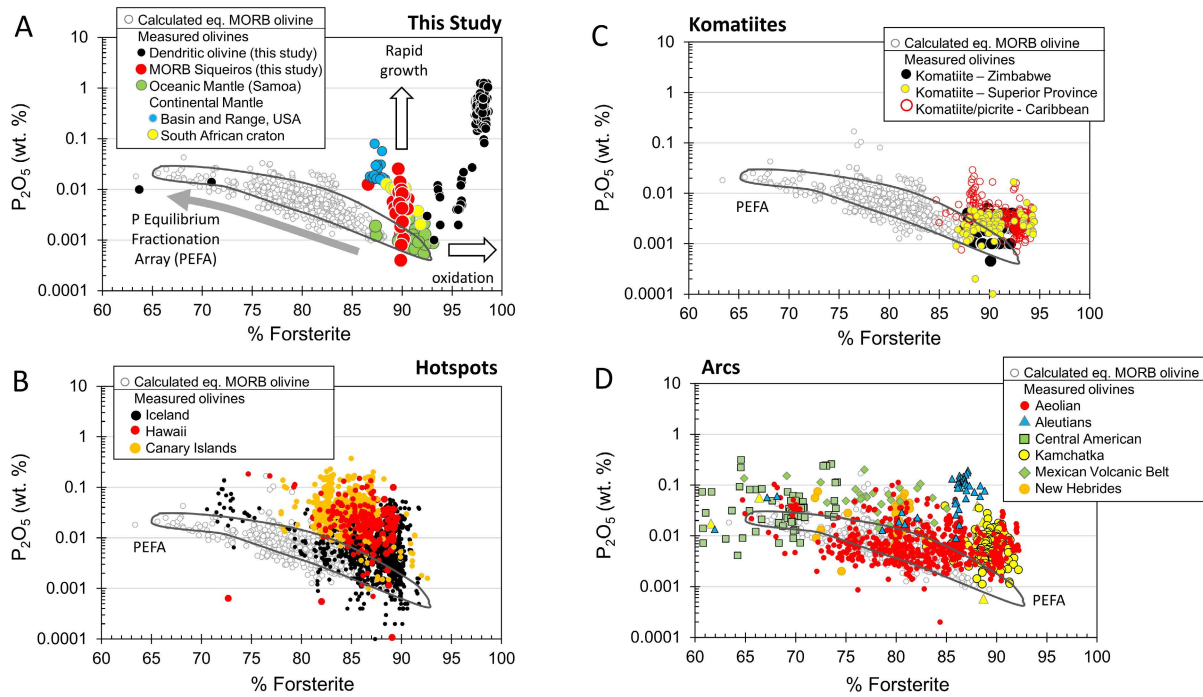
Figure 6: Olivine P_2O_5 concentration versus forsterite content (atomic Mg/(Mg+Fe)×100). [A] Results of this study and that of He et al. [2019]. Black symbols represent dendritic olivine phenocrysts from Kaua'i and red symbols represent olivine phenocrysts from Siqueiros MORB glass investigated here. Also shown are olivines from mantle xenoliths representing oceanic lithospheric mantle (Samoa oceanic island) and continental lithospheric mantle (Phanerozoic Basin and Range in USA and Archean Kaapvaal Craton in southern Africa) from He et al. [2019]. Open gray circles represent calculated olivine compositions in equilibrium with MORB glass compositions from global compilation of Jenner and O'Neill [2012]. Equilibrium olivine compositions calculated assuming a temperature-corrected P partition coefficient (see text). The array of equilibrium olivine compositions is outlined and defined as the Phosphorous Equilibrium Fractionation Array (PEFA); gray arrow shows direction of differentiation. Horizontal white arrows show direction of oxidation. Vertical white arrow shows direction of rapid growth. The unique spinifex olivines from Kaua'i can be explained by rapid crystal growth under oxidizing conditions. [B] Olivine phenocryst compositions from basalts from Iceland, Hawai'i and the Canary Islands. All other symbols as in [A]. [C] Olivine phenocrysts from Archean (Zimbabwe and Superior Province) and Phanerozoic (Gorgona) komatiites. All other symbols as in [A]. [D] Olivine phenocrysts from various arc magmas. All other symbols as in [A].

rium line for MORBs, which we term the Phosphorous Equilibrium Fractionation Array (PEFA)

$$C_{P_2O_5} = 458.6e^{-0.1409Fo} \qquad (2)$$

We define deviations from the MORB PEFA for a given Fo as $\Delta PEFA = \log_{10}(C/C_o)$, so that $\Delta PEFA = 0$ is at equilibrium. Every integer unit of $\Delta PEFA$ represents a factor of 10 (Figures 6 and 7). We note that the correlation coefficient for this regression is low ($r^2 = 0.43$), so there are large uncertainties in $\Delta PEFA$. Unfortunately, at this point in time, we cannot do better than this. Uncertainties in PEFA could stem from natural variability but also uncertainties in P measurements from the compiled literature, which is difficult to fully assess. Despite these uncertainties, we hope that we have provided the framework for improving the accuracy of PEFA. Regardless, as we show below, deviations of natural olivines from PEFA can be orders of magnitude and are thus real.

We now return to the measured P contents of olivine crystals. Two important features are apparent. First, for a given Fo content, P can vary by more than a factor of 10 for olivines from Siqueiros MORB, arcs, and oceanic islands (Figure 6). Such variation, if due to far-field equilibrium, would require complementary melt compositions to vary by the same amount, but the P contents of the magmas hosting these olivines show much less variation in P for a given melt Mg/(Mg+Fe). The olivine crystal data alone indicate a large component of the olivines are in disequilibrium. The second observation is that despite the variability in olivine P contents, the lowest measured P contents are generally bounded below by the PEFA ($\Delta PEFA \sim 0$) so that the majority of olivines have $\Delta PEFA > 0$ (Figure 7A). None of the P enrichments approaches the extreme enrichments in the dendritic olivines from Kaua'i, Hawai'i discussed above, but the lowest P concentrations of the dendritic olivines are still bounded below by PEFA.

Remarkably, the majority of olivines from basaltic magmas across most magmatic environments are in disequilibrium in terms of the MORB PEFA and do not reflect the composition of the host magma, instead reflecting kinetic processes. Oceanic islands show the most disequilibrium, with P contents >10 times higher than PEFA, similar to MORBs as sampled by Siqueiros olivines in this study (Figures 6 and 7A). We
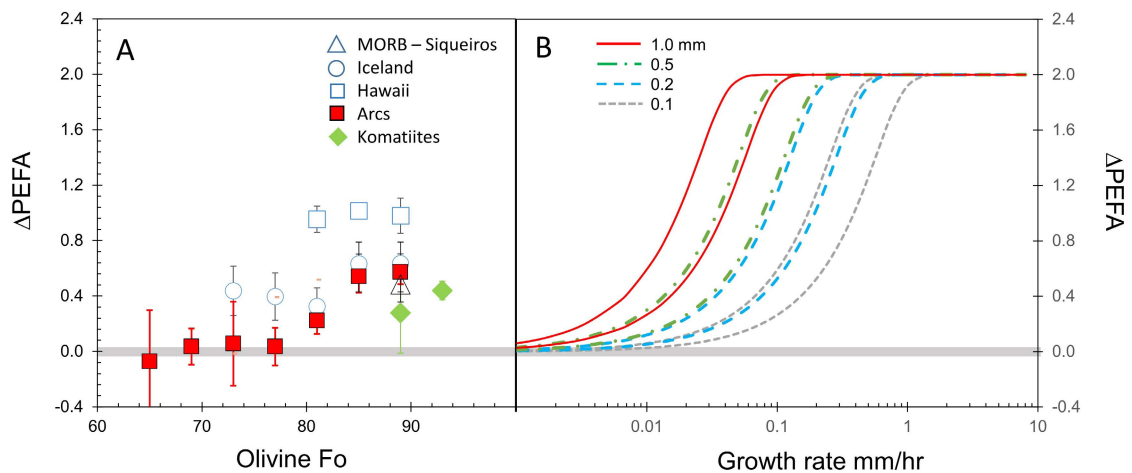
Figure 7: [A] Deviations from PEFA in units of ΔPEFA for olivines from different magmatic environments. ΔPEFA values represent the mean over 2 units of forsterite. Vertical error bars represent 3 standard errors of the mean, where standard error is the standard deviation divided by the square root of the number of samples. [B] Results of crystal growth models, where the extent of disequilibrium as represented by ΔPEFA is plotted against crystal growth rate. Colors represent different assumed boundary layer thicknesses in the melt. For a given color (boundary layer thickness), left line corresponds to P diffusivity at 1180 °C and right line at 1250 °C.

also examined olivines from two Archean komatiite flows and a unique Phanerozoic komatiite. Their P contents range from PEFA to <5 times PEFA and are thus the closest to equilibrium of the magmas discussed here.

The extent of disequilibrium appears to be lower in subduction zone magmas (arc magmas). Primitive arc magmas are 5–10 times higher than the MORB-defined PEFA, but for more evolved arc magmas, such as basaltic andesites and olivine-bearing andesites, many fall on the MORB-defined PEFA. This may indicate a closer approach to equilibrium for more evolved arc magmas, although we note that the MORB-defined PEFA line may not be perfectly applicable to arc magmas that undergo calc-alkaline differentiation. Under calc-alkaline differentiation, the decrease in melt Mg# is less for a given extent of crystallization, so the MORB-based PEFA may be underestimated. If so, ΔPEFAs estimated for evolved arc magma olivines are maximum bounds, and arc magma olivines may be even closer to equilibrium in terms of P than shown here.

6 FROM DISEQUILIBRIUM TO RATES OF CRYSTAL GROWTH AND MAGMA COOLING

Deviations from PEFA reflect disequilibrium. Here, we interpret such disequilibria through the framework of transport limited kinetics, that is, disequilibrium is due to high Peclet number during crystal growth, which is a measure of the relative rates of crystal growth and diffusional relaxation in the melt. Exactly what causes the differences between these effective Peclet numbers is unclear. One possible explanation for the larger ΔPEFA in ocean islands and MORBs compared to arcs is that the more hydrous compositions of arc magmas increase chemical diffusivities in the melt. This may be an attractive hypothesis because the water contents of arc magmas increase with differentiation and, indeed, it appears that arc magmas approach P equilibrium with progressive differentiation. However, differentiation is accompanied by cooling,

which decreases diffusivities. The temperature effect on diffusivity is also stronger than the effect of water [Zhang et al. 2010].

Deviation from PEFA may be more likely controlled by rapid crystal growth. To quantify crystal growth from P in olivine requires an estimate of P diffusivity in the melt [Watson et al. 2015] and an estimate of the thickness of the P-enriched boundary layer in the melt. The former depends on the temperature at which the olivine crystallized, which we obtain empirically from the equilibrium MORB olivine array and the MgO content of the corresponding melt. We have no direct constraints on P boundary layer thicknesses in our global olivine crystal database as this quantity is rarely ever measured. However, we can place bounds on the boundary layer thickness. For a growing spherical crystal (approximating an equant olivine grain) under locally static melt conditions (i.e. where the Reynold's number is zero), the melt boundary layer thickness should be of the same order as the radius of the crystal (Chapter 5 in Lewis et al. [2015]). Most of the olivine grains analyzed are of 1–2 mm, so we take 1 mm as an approximation of the boundary layer thickness for growth. In Figure 7B, ΔPEFA is plotted against growth for different boundary layer thicknesses and two temperatures: a high end, defining primitive magmas (1250 °C) and a low end, defining evolved basalts (1180 °C). For the ΔPEFAs reported, we find that growth rates lie between 0.01 and 0.1 mm/h. Higher growth rates would be possible if the conditions were turbulent (Reynold's number $>10^3$) and boundary layer thicknesses were much thinner. Turbulent scenarios may occur during pegmatite formation [Phelps et al. 2020], but for basaltic to felsic magmas at the scale of a phenocryst, laminar flow (i.e. low Reynold's number) dominates.

The question now is what causes the rapid crystal growth? The driving force for crystal growth is supersaturation, which for magmatic crystallization is largely controlled by the de-
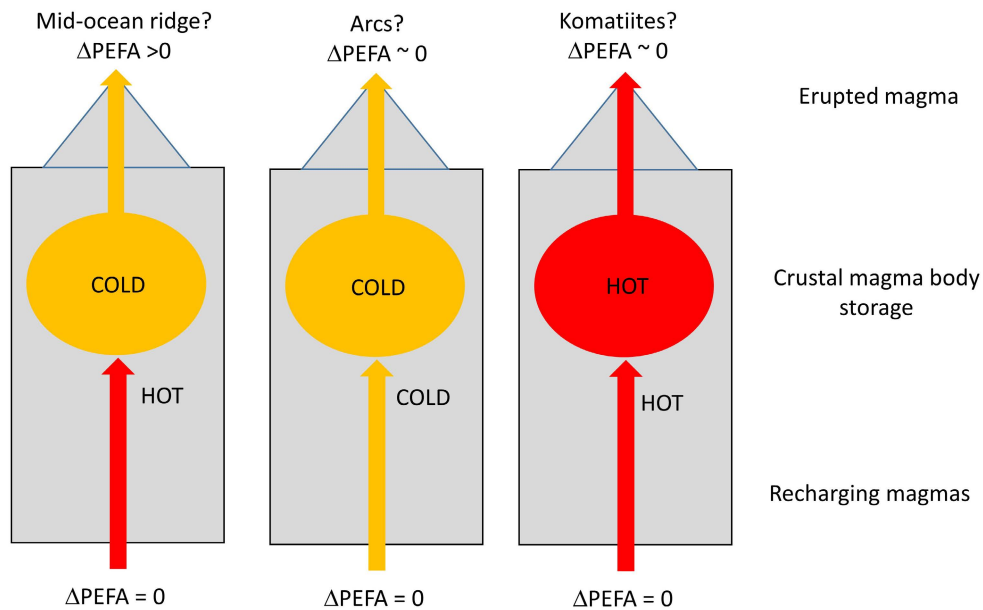
Figure 8: Scenario 1 for explaining differences in disequilibria. Disequilibria reflects temperature contrast between recharging magmas and crustal magma bodies where magmas reside and are stored. Large temperature contrasts between recharging magma and storage zones result in rapid cooling of the recharged magma, causing large disequilibrium (ΔPEFA >0). In mid-ocean ridge environments, recharging magmas may be more primitive and hotter than the crustal magma body. In arcs, both the crustal magma body and recharging magmas might be evolved and cold, resulting in low temperature contrast and slower cooling rates. In komatiites, magma bodies and recharging magmas are both hot, resulting in low temperature contrast and slower cooling rates.

gree of undercooling with respect to the liquidus. Without undercooling, crystallization takes place at near equilibrium conditions, and both nucleation and growth are slow. We parameterize olivine crystallization experiments [Jambon et al. 1992] to convert crystal growth rates to degree of undercooling ΔT (°C)

$$G = 1.076 \times 10^{-10}(\Delta T)^{1.878} \tag{3}$$

which has units of m/s (Figure 8A). More recent experiments are broadly consistent with this parameterization [Mourey and Shea 2019]. Estimates of G can be used with this equation to estimate an effective average undercooling ΔT (Figure 8A). We can then use the radius of an olivine grain and divide by G to estimate the elapsed time Δt for olivine growth, allowing estimation of the effective cooling rate dT/dt during olivine growth. For radii of 1 to 5 mm, we estimate cooling rates during olivine growth in OIBs and MORBs to be approximately between ~10^2 and 5×10^3 °C/y. For arc olivines, cooling rates appear to be slower, <10^3 °C/y, although because many arc magmas approach equilibrium, we do not have a lower bound on cooling rates. These are clearly very crude estimates of cooling rate because the exact dependency of growth rate on degree of undercooling depends on the diffusivity of essential structural components (e.g. Mg and Si for olivine) in the melt, which in turn depends on the composition and temperature of the melt [Mourey and Shea 2019]. To properly expand this to different magmatic systems in the future will require growth curves for specific magma types.

7 THE SIGNIFICANCE OF RAPID COOLING IN MAGMA BODIES

What the above cooling rates mean in terms of magma dynamics is unclear. We consider a few possibilities. Two scenarios come to mind if cooling rates are related only to the growth of the olivine and not to the overall thermal history of the magma body. In one scenario, cooling rate may provide insight into the temperature contrast between a crustal magma body and recharging magmas. In a second scenario, cooling rates may reflect local conditions, such as cooling on the margins of a magma body. A third scenario comes to mind if the cooling rates reflect the time-averaged cooling of the magma body. In this case, there are implications for the length scales of magma bodies.

7.1 Scenario 1: Large temperature contrast between crustal magma bodies and recharging magmas

Strictly speaking, any inferred cooling rate from olivine phenocrysts reflects the thermal history during the interval over which an olivine crystal grew. That is, once an olivine crystal stops growing, it stops recording any further history of the magma, but otherwise remains intact for the remaining lifetime of the magma. In this scenario, cooling rates inferred from olivine phenocrysts reflect only the conditions that triggered olivine crystallization. We can envision a long-lived magma body that is periodically being recharged by a more primitive and hotter magma as has been suggested for Hawaiʻi [Pietruszka et al. 2015] (Figure 8). If so, rapid cooling rates might suggest a strong temperature contrast between recharg-
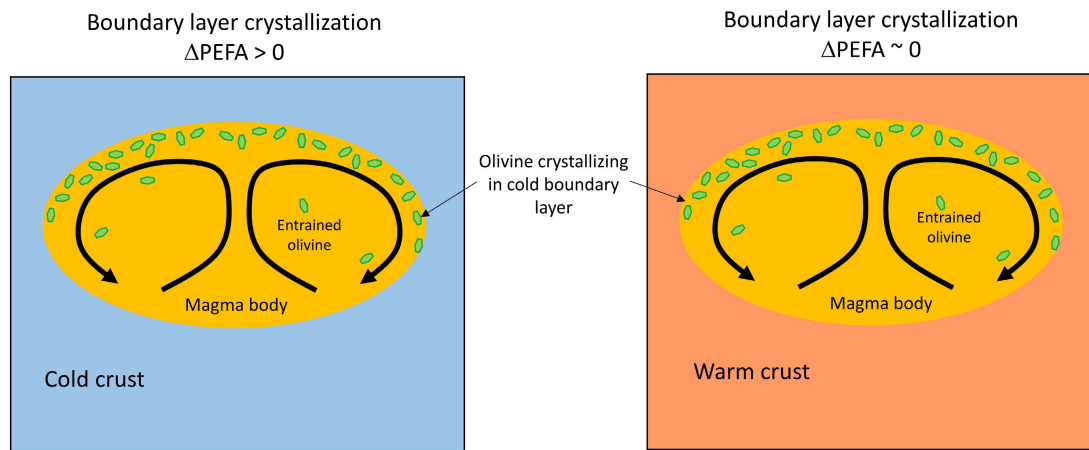
Figure 9: Scenario 2 where olivines crystallize in the cold boundary layers of large, long-lived magma chambers and then get re-entrained into the magma body. Temperature contrast between magma body and crust control cooling rate in the boundary layer. Deep-seated magma bodies in arc systems may display lower temperature contrast with the crustal wall rock, resulting in slower cooling. In contrast, shallow magma bodies, such as in mid-ocean ridge environments, might be surrounded by cold crust, resulting in rapid cooling.

ing magma and the magma body, forcing the recharging magma to quickly cool and crystallize olivine (pers. comm., P. Wieser). In this context, mid-ocean ridge and ocean island environments, which show the highest cooling rates, are sourced from magma bodies in which the recharging magma is considerably hotter than the crustal magma body. The slower cooling rates inferred for arc magma olivines might suggest that the temperatures of the recharging magmas are like that of the crustal magma bodies into which the magmas intrude. These conclusions seem reasonable if recharging magmas in mid-ocean ridge systems are more primitive or generally hotter than those in arc systems. Komatiites, which are closer to equilibrium, might suggest that both the magma body and replenishing magmas are primitive and hot. Unfortunately, because we have no constraints on the length scales of recharging magmas, we cannot expand on this hypothesis more quantitatively.

7.2 Scenario 2: Olivines crystallize on magma body margins

Another possibility for rapid cooling is that olivine crystallization occurs locally, perhaps on the margins of magma bodies where the magma can chill (i.e. boundary layer crystallization) (Figure 9). These olivines then get re-incorporated into the main magma body through convection or re-entrainment of accumulated crystals [Bradshaw et al. 2018]. In this scenario, olivines re-entrained into the core of a magma body and stored should heat back up or possibly react with more primitive melts. Such olivines would be predicted to show resorption or reverse zonation [Pankhurst et al. 2018]. Reverse zoning is often interpreted as evidence for a recharging event, but if boundary layer crystallization is important, such zoning could simply be the result of boundary layer olivines migrating into the interior of a larger, longer-lived magma body [Pankhurst et al. 2018].

In any case, within the framework of this scenario, the more rapid cooling rates in mid-ocean ridge and oceanic island envi-

ronments might suggest strong temperature contrast between magma bodies and crustal wall rock. The slower cooling rates inferred for arc magmas might indicate smaller temperature contrasts between crustal magma bodies and the wall rock in arc environments, consistent with deeper magma bodies in the thick crust of arcs. The minimal disequilibrium seen in komatiites, however, probably cannot be explained with this scenario.

7.3 Scenario 3: Magma bodies are small

If these cooling rates instead reflect the thermal history of a magma body, the fast cooling rates might suggest that the magma bodies must be of small length scale (Figure 10). To explore this further, we consider the case in which magmas are emplaced as tabular bodies, wherein cooling is controlled primarily by conduction. The time-averaged cooling rate in the center of such a body is approximated by

$$\frac{dT}{dt} \sim \frac{a\kappa}{H^2} \qquad (4)$$

where κ is thermal diffusivity (m^2/s), H is the thickness of the sill, and a is an empirical constant (°C) related to the magma/wall rock temperature difference and the temperature range over which olivine crystallizes. This empirical term is determined from modeling thermal conduction over a symmetric infinite half-space [Carslaw and Jaeger 1959] and assuming a basalt liquidus temperature of 1200 °C, a wall rock temperature of 600 °C, and the average temperature interval over which olivine crystallizes (1200–1000 °C). This gives a value of a of 200 °C/0.53. Importantly, the cooling rate dT/dt is most sensitive to variations in H. Variability in a is limited because the wall rock/magma temperature difference and the temperature range over which olivine crystallizes does not vary significantly. If dT/dt is known from growth rate G, we can estimate the thickness of the magmatic body. Figure 11B shows thickness of a magma body versus crystal
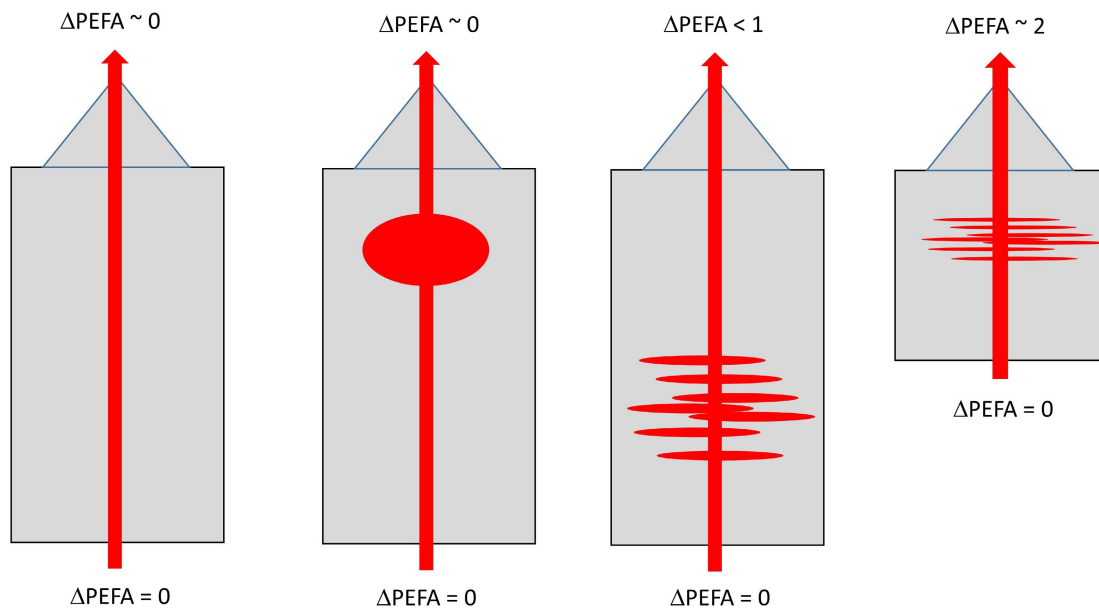
Figure 10: Cartoons depicting different types of magmatic plumbing systems and qualitative predictions on the degree of disequilibrium expressed in terms of ΔPEFA. We assume that ΔPEFA = 0 in the mantle melting regime due to the high temperatures and limited mobility of the melts. Once melts leave their mantle sources, they may transit to the surface in different ways. From left to right, direct transit to the surface, staging in a large crustal magma chamber, staging as sills in lower crust, and staging as sills in the upper crust. Direct transit to the surface may preserve ΔPEFA = 0 from the mantle as exemplified by komatiites, many of which are near-primary mantle-derived melts. In crustal staging, rapid cooling will lead is ΔPEFA >0 as in the case of small sills in the crust. Large magma chambers cool more slowly and would have intermediate ΔPEFA.
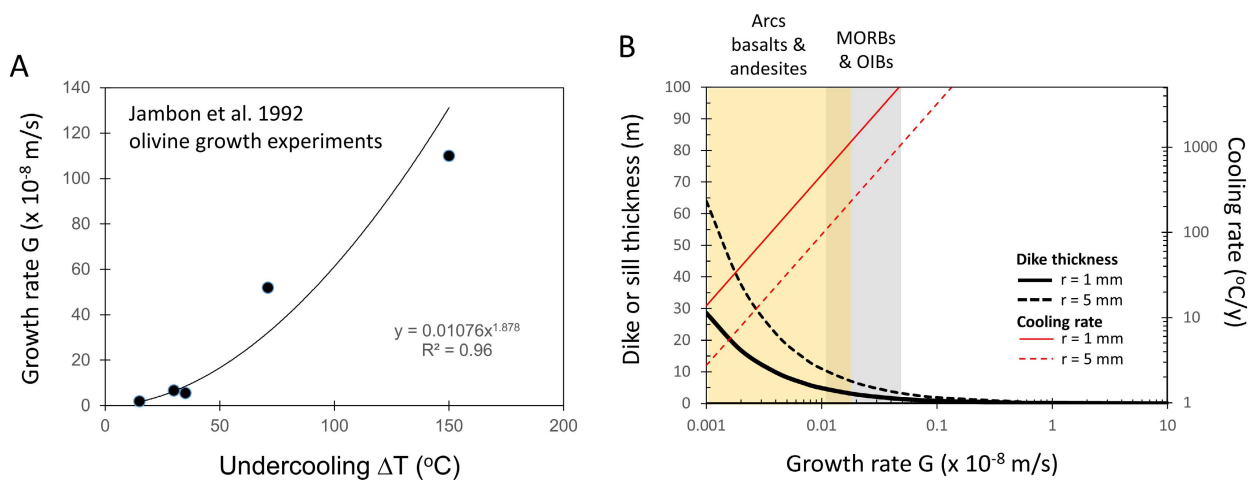
Figure 11: [A] Olivine growth experiments of Jambon et al. [1992] showing growth rate versus degree of undercooling, e.g. temperature below liquidus. Curved line represents a regression of the data using an exponential function. [B]Model results showing how growth rate relates to dike/sill thickness (black bold lines) and initial cooling rate (thin red lines). Left hand axis refers to dike/sill thickness and right-hand axis for cooling rate. Dashed lines correspond to the hypothetical case in which characteristic olivine radius is 5 mm. Solid lines are for olivine radius of 1 mm, which is the typical length scale of olivine phenocrysts. Note that cooling rate corresponds to the effective cooling rate over which olivine grows and does not reflect the long-term cooling rate of the dike. Vertical shaded regions correspond to the range of growth rates estimated from ΔPEFA in Figure 5.

growth rate for different characteristic radii of olivine crystals (1 and 5 mm). As discussed above, we use the radii to estimate elapsed time.

Ranges of crystal growth rates for oceanic islands, arcs and mid-ocean ridges based on their ΔPEFA values from Figure 7 are shown in Figure 8B for comparison. Using these numbers, we predict magma thicknesses of <5 m in mid-ocean ridge systems and oceanic islands and between 10–70 m for basaltic magmas in arcs and greater than 100 m for andesitic magmas in arcs. For more evolved arc magmas and komati-

ites, ΔPEFA approaches zero. For arcs, this may suggest longer cooling times, which could be because arc magma bodies are thicker or deeper in the crust. It is also possible that the crustal incubation zones for arc magmas are subjected to longer intervals of magmatic fluxing, prolonging cooling times [Karakas et al. 2017], which our simple thermal model does not account for.

In any case, the length scales of magma bodies inferred here are much smaller than the scales of plutons. If correct, the large km-scale magma bodies envisaged in the literature [Bachmann 2004; Hildreth and Wilson 2007] may instead be made up of numerous small sills, possibly emplaced over a protracted period of time [Halliday et al. 1989; Glazner et al. 2004; Simon and Reid 2005; Barboni et al. 2015] (Figure 9). Indeed, seismic studies of crustal magmatic systems have never imaged a magmatic body with over 25 % melt; most cases are <10 % melt [Nicolas et al. 1993; Ward et al. 2014; Huang et al. 2015; Delph et al. 2017]. A large, mostly solid region interspersed with thin high melt-fraction sills might be indistinguishable geophysically from a large partially molten magma body (Figure 9).

8 FUTURE WORK

In summary, our work shows that the P contents of most olivine crystals in magmatic systems are in disequilibrium. What controls the extent of disequilibrium is unclear, but rapid crystal growth and cooling seem likely. What these inferred cooling rates mean in terms of magma system dynamics is unclear, but rapid cooling suggests that olivine crystallization either reflects very local processes/events in large, long-lived magma bodies or that the magma bodies themselves are small and short-lived.

It would be worth extending our approach to olivines in continental intraplate magmas or even to olivines in Martian and lunar meteorites and beyond. We also envision extending these concepts to other elements, such as Na, Ti, and Al. Because of their different diffusivities, a multi-element study may help reduce uncertainties in estimates of crystal growth rates. Investigating other minerals would provide insight into other types of magmatic systems. Detailed studies of quartz and feldspar phenocrysts, for example, may provide insights into how felsic plutons, particularly those that generate ore-bearing porphyries or large silicic eruptions, are assembled.

In the end, nature is complicated. In our attempt to simplify, we admit that many of our interpretations here may be wrong. What is correct is that most garden variety olivine crystals in magmas are in disequilibrium in terms of P. What may not be correct is our inference of crystal growth rates and extension to cooling rates. Uncertainties in crystal growth rate modeling depend on assumed boundary layer thicknesses, constant growth rates, and idealized crystal geometries, as well as uncertainties in equilibrium partition coefficients and chemical diffusivities. It is also possible that attachment kinetics are equally if not more important than transport-limited kinetics, in which case, none of the kinetic modeling applied in this paper is relevant to explaining the observed trace-element disequilibria. Finally, our interpretation of cooling rates in the context of magma dynamics is obviously non-unique. We wish we had all the answers, but we leave behind unresolved questions and perplexing observations.

9 METHODS

Mineral compositions were analyzed using a Jeol JXA8530F Hyperprobe electron probe micro-analyzer (EPMA) in the Department of Earth, Environmental and Planetary Sciences at Rice University. The EPMA is equipped with a field emission assisted thermo-ionic (Schottky) emitter, and five Wavelength Dispersive Spectrometers (WDS). Analyses were performed using a 15 kV accelerating voltage and a 50 nA beam current with a spot beam size of ~250 nm. The counting time used in measuring the characteristic X-rays of elements present in olivine were 20 s for Si, Mg, and Fe (10 s/peak and 5 s for each upper and lower background); 100 s for Ca, Ti, Cr, Al, Mn, and Ni (40 s/peak and 30 s for each upper and lower background). For P, a counting time of 160 s was used (60 s/peak and 50 s for each upper and lower background), obtaining an average detection limit of 12 ppm and average analytical standard deviation (1σ) of 2.3 %. Natural minerals were used for calibration: olivine (Fo93) for Si, Mg, and Fe, diopside for Ca, plagioclase for Al, rutile for Ti, chromite for Cr, rhodonite for Mn, jadeite for Na, pentlandite for Ni, and apatite for P. Calibration standards were obtained from SPI Supplies (Mount 02753-AB). Sensitive analyzing crystals were used to analyze elements with lower concentration: LLiF and/or LiFH for Cr, Mn and Ni, and PETL for P. The PRZ (Jeol) matrix correction was employed for quantification. For details regarding spectrometer, detector conditions and background offsets for all analyzed elements, see Supplementary tables. Wavelength Dispersive Spectrometry (WDS) element mapping was acquired using 15 kV accelerating voltage, 150 nA beam current, 30 ms dwell time, and stage mode scanning. Deadtime correction was applied for each element map. All major elements are reproduced with internal precision <2 %. Minor elements are reproduced within 3–5 %. Phosphorous (P_2O_5) was measured against Smithsonian basalt glass standard with 0.29 P_2O_5 with a reproducibility within 3 % (NMNH-113716-1). P detection limits were less than 15 ppm (as elemental). Additional calibration details are in the Supplementary tables.

10 SAMPLES AND LITERATURE DATA

Data from this study and compiled from the literature are in Supplementary tables.

10.1 Kaua'i, Hawai'i (this study)

Olivines from Kaua'i, HI are from samples collected by Dana Johnston [Johnston and Stout 1984a; b; Johnston et al. 1985; Johnston and Beckett 1986].

10.2 Siqueiros data (this study)

Olivine data from MORBs are from this study and refer solely to Siqueiros along the East Pacific Rise. We analyzed olivines from glassy picrites from sites 2384 (3, 6, 8) and D20-1 as outlined in Perfit et al. [1996]. The samples were gently crushed and olivine grains were extracted. Olivines were mounted in epoxy, polished, and then analyzed by EPMA using the an-

alytical protocols described above. We made no attempt to remove any glass rinds from the olivines as our goal was to measure the olivine cores, rims and adjacent glass.

10.3 Literature data

Phosphorous is commonly reported for olivine. However, P_2O_5 contents, traditionally determined by EPMA, are usually reported only to the second decimal (e.g. 0.01 wt. % P_2O_5). Because P_2O_5 concentrations in most olivines are typically less than 0.01 wt. %, most of the historical data have uncertainties or detection limits too high to be useful for this study. As noted in Section 9, however, detection limits by EPMA can be lowered if longer count times are adopted. We thus compiled EPMA data only from sources in which detection limits approached 0.002 wt. % P_2O_5. In cases where EPMA detection limits were not explicitly reported, we sought data sources in which reported P_2O_5 concentrations included measurements <0.005 wt. %. We also incorporated P data determined by laser ablation ICP-MS, which has detection limits for P_2O_5 <0.001 wt. % [He et al. 2019].

Olivine data for ocean island basalts (OIBs) are as follows: Canary Islands [Gómez-Ulla et al. 2017], Hawai'i [Rae et al. 2016; Putirka et al. 2018], Iceland [Neave et al. 2015; 2018; Nikkola et al. 2019a; b; Rasmussen et al. 2020]. Olivine data for arcs are as follows: Aleutians [Zimmer et al. 2010], Aeolian Arc [Zamboni et al. 2017], Central America [Liu et al. 2020], Kamchatka [Zelenski et al. 2018], Mexican Volcanic Belt [Losantos et al. 2017], New Hebrides [Beier et al. 2018]. Olivine data from komatiites are as follows: Caribbean-Colombian Plateau [Trela et al. 2017; Asafov et al. 2018], Superior Province [Sobolev et al. 2016], Zimbabwe [Asafov et al. 2018].

Olivine data for Samoa mantle xenoliths, which we take to represent pristine oceanic lithospheric mantle, come from He et al. [2019]. We also report olivines from Phanerozoic continental lithospheric mantle in the Basin and Range Province, USA and Archean cratonic mantle from South Africa [He et al. 2019].

The only P measurements for MORB olivines used in this study pertain to our own measurements on Siqueiros picrites (see above). As discussed in main text, hypothetical olivine compositions in equilibrium with MORBs were calculated from MORB glass [Jenner and O'Neill 2012] by dividing by an equilibrium partition coefficient as described in the main text.

10.4 Diffusion parameters

Diffusion parameters in basaltic melt were taken from recent compilations [Zhang et al. 2010]: Ti ($\ln D_o$ = -8.92 m^2/s, E_A/R = 2.55×10^4 K [Chen and Zhang 2008]), Al ($\ln D_o$ = -5.75 m^2/s, E_A/R = 3.13×10^4 K [Chen and Zhang 2008]), Ni ($\ln D_o$ = -1.87 m^2/s, E_A/R = 3.73×10^4 K [Behrens and Hahn 2009]), Mn ($\ln D_o$ = -13.5 m^2/s, E_A/R = 1.62×10^4 K [Lowry et al. 1982], Ca ($\ln D_o$ = -10.5 m^2/s, E_A/R = 2.12×10^4 K [Chen and Zhang 2009]), Na ($\ln D_o$ = -9.32 m^2/s, E_A/R = 1.97×10^4 K [Lowry et al. 1982]), and P ($\ln D_o$ = -14.5 m^2/s, E_A/R = 1.77×10^4 K [Watson et al. 2015].

References

Adam, J. and T. Green (2006). "Trace element partitioning between mica- and amphibole-bearing garnet lherzolite and hydrous basanitic melt: 1. Experimental results and the investigation of controls on partitioning behaviour". *Contributions to Mineralogy and Petrology* 152(1), pages 1–17. DOI: 10.1007/s00410-006-0085-4.

Anderson, A. and L. Greenland (1969). "Phosphorus fractionation diagram as a quantitative indicator of crystallization differentiation of basaltic liquids". *Geochimica et Cosmochimica Acta* 33(4), pages 493–505. DOI: 10.1016/0016-7037(69)90129-x.

Asafov, E., A. Sobolev, A. Gurenko, N. Arndt, V. Batanova, M. Portnyagin, D. Garbe-Schönberg, and S. Krasheninnikov (2018). "Belingwe komatiites (2.7 Ga) originate from a plume with moderate water content, as inferred from inclusions in olivine". *Chemical Geology* 478, pages 39–59. DOI: 10.1016/j.chemgeo.2017.11.002.

Bachmann, O. (2004). "On the Origin of Crystal-poor Rhyolites: Extracted from Batholithic Crystal Mushes". *Journal of Petrology* 45(8), pages 1565–1582. DOI: 10.1093/petrology/egh019.

Bacon, C. R. (1989). "Crystallization of accessory phases in magmas by local saturation adjacent to phenocrysts". *Geochimica et Cosmochimica Acta* 53(5), pages 1055–1066. DOI: 10.1016/0016-7037(89)90210-x.

Barboni, M., C. Annen, and B. Schoene (2015). "Evaluating the construction and evolution of upper crustal magma reservoirs with coupled U/Pb zircon geochronology and thermal modeling: A case study from the Mt. Capanne pluton (Elba, Italy)". *Earth and Planetary Science Letters* 432, pages 436–448. DOI: 10.1016/j.epsl.2015.09.043.

Baziotis, I., P. D. Asimow, T. Ntaflos, J. W. Boyce, F. M. McCubbin, A. Koroneos, D. Perugini, S. Flude, M. Storey, Y. S. Liu, S. Klemme, and J. Berndt (2017). "Phosphorus zoning as a recorder of crystal growth kinetics: application to second-generation olivine in mantle xenoliths from the Cima Volcanic Field". *Contributions to Mineralogy and Petrology* 172(7). DOI: 10.1007/s00410-017-1376-7.

Baziotis, I., S. Xydous, P. Asimow, C. Mavrogonatos, S. Flemetakis, S. Klemme, and J. Berndt (2019). "The potential of phosphorus in clinopyroxene as a geospeedometer: Examples from mantle xenoliths". *Geochimica et Cosmochimica Acta* 266, pages 307–331. DOI: 10.1016/j.gca.2019.04.024.

Behrens, H. and M. Hahn (2009). "Trace element diffusion and viscous flow in potassium-rich trachytic and phonolitic melts". *Chemical Geology* 259(1-2), pages 63–77. DOI: 10.1016/j.chemgeo.2008.10.014.

Beier, C., P. A. Brandl, S. M. Lima, and K. M. Haase (2018). "Tectonic control on the genesis of magmas in the New Hebrides arc (Vanuatu)". *Lithos* 312-313, pages 290–307. DOI: 10.1016/j.lithos.2018.05.011.

Boesenberg, J. S. and R. H. Hewins (2010). "An experimental investigation into the metastable formation of phosphoran olivine and pyroxene". *Geochimica et Cosmochimica Acta* 74(6), pages 1923–1941. DOI: 10.1016/j.gca.2009.12.008.

Bradshaw, R. W., A. J. Kent, and F. J. Tepley (2018). "Chemical fingerprints and residence times of olivine in the 1959 Kilauea Iki eruption, Hawaii: Insights into picrite formation". *American Mineralogist* 103(11), pages 1812–1826. DOI: 10.2138/am-2018-6331.

Brunet, F. and G. Chazot (2001). "Partitioning of phosphorus between olivine, clinopyroxene and silicate glass in a spinel lherzolite xenolith from Yemen". *Chemical Geology* 176(1-4), pages 51–72. DOI: 10.1016/s0009-2541(00)00351-x.

Burton, J. A., R. C. Prim, and W. P. Slichter (1953). "The Distribution of Solute in Crystals Grown from the Melt. Part I. Theoretical". *The Journal of Chemical Physics* 21(11), pages 1987–1991. DOI: 10.1063/1.1698728.

Carslaw, H. S. and J. C. Jaeger (1959). *Conduction of Heat in Solids*. 2nd edition. Oxford University Press, Amen House, London EC4: Oxford University Press. ISBN: 0198533683.

Chen, Y. and Y. Zhang (2008). "Olivine dissolution in basaltic melt". *Geochimica et Cosmochimica Acta* 72(19), pages 4756–4777. DOI: 10.1016/j.gca.2008.07.014.

– (2009). "Clinopyroxene dissolution in basaltic melt". *Geochimica et Cosmochimica Acta* 73(19), pages 5730–5747. DOI: 10.1016/j.gca.2009.06.016.

Delph, J. R., K. M. Ward, G. Zandt, M. N. Ducea, and S. L. Beck (2017). "Imaging a magma plumbing system from MASH zone to magma reservoir". *Earth and Planetary Science Letters* 457, pages 313–324. DOI: 10.1016/j.epsl.2016.10.008.

Demouchy, S. and S. Mackwell (2006). "Mechanisms of hydrogen incorporation and diffusion in iron-bearing olivine". *Physics and Chemistry of Minerals* 33(5), pages 347–355. DOI: 10.1007/s00269-006-0081-2.

DePaolo, D. J. (1981). "Trace element and isotopic effects of combined wallrock assimilation and fractional crystallization". *Earth and Planetary Science Letters* 53(2), pages 189–202. DOI: 10.1016/0012-821x(81)90153-9.

Edmonds, M., K. V. Cashman, M. Holness, and M. Jackson (2019). "Architecture and dynamics of magma reservoirs". *Philosophical Transactions of the Royal Society A: Mathematical, Physical and Engineering Sciences* 377(2139), page 20180298. DOI: 10.1098/rsta.2018.0298.

Faure, F. (2006). "Formation of Spinifex Texture in Komatiites: an Experimental Study". *Journal of Petrology* 47(8), pages 1591–1610. DOI: 10.1093/petrology/egl021.

Foley, S. F., D. E. Jacob, and H. S. C. O'Neill (2010). "Trace element variations in olivine phenocrysts from Ugandan potassic rocks as clues to the chemical characteristics of parental magmas". *Contributions to Mineralogy and Petrology* 162(1), pages 1–20. DOI: 10.1007/s00410-010-0579-y.

Glazner, A. F., J. M. Bartley, D. S. Coleman, W. Gray, and R. Z. Taylor (2004). "Are plutons assembled over millions of years by amalgamation from small magma chambers?" *GSA Today* 14(4), page 4. DOI: 10.1130/1052-5173(2004)014<0004:apaomo>2.0.co;2.

Gómez-Ulla, A., O. Sigmarsson, and G. H. Gudfinnsson (2017). "Trace element systematics of olivine from historical eruptions of Lanzarote, Canary Islands: Constraints on mantle source and melting mode". *Chemical Geology* 449, pages 99–111. DOI: 10.1016/j.chemgeo.2016.11.021.

Grant, T. B. and S. C. Kohn (2013). "Phosphorus partitioning between olivine and melt: An experimental study in the system Mg2SiO4-Ca2Al2Si2O9-NaAlSi3O8-Mg3(PO4)2". *American Mineralogist* 98(10), pages 1860–1869. DOI: 10.2138/am.2013.4237.

Grove, T. L. and T. C. Juster (1989). "Experimental investigations of low-Ca pyroxene stability and olivine-pyroxene-liquid equilibria at 1-atm in natural basaltic and andesitic liquids". *Contributions to Mineralogy and Petrology* 103(3), pages 287–305. DOI: 10.1007/bf00402916.

Halliday, A., G. Mahood, P. Holden, J. Metz, T. Dempster, and J. Davidson (1989). "Evidence for long residence times of rhyolitic magma in the Long Valley magmatic system: the isotopic record in precaldera lavas of Glass Mountain". *Earth and Planetary Science Letters* 94(3-4), pages 274–290. DOI: 10.1016/0012-821x(89)90146-5.

He, D., C.-T. A. Lee, X. Yu, and M. Farner (2019). "Ge/Si Partitioning in Igneous Systems: Constraints From Laser Ablation ICP-MS Measurements on Natural Samples". *Geochemistry, Geophysics, Geosystems* 20(10), pages 4472–4486. DOI: 10.1029/2019gc008514.

Hildreth, W. and S. Moorbath (1988). "Crustal contributions to arc magmatism in the Andes of Central Chile". *Contributions to Mineralogy and Petrology* 98(4), pages 455–489. DOI: 10.1007/bf00372365.

Hildreth, W. and C. J. N. Wilson (2007). "Compositional Zoning of the Bishop Tuff". *Journal of Petrology* 48(5), pages 951–999. DOI: 10.1093/petrology/egm007.

Hofmann, A. W. (1988). "Chemical differentiation of the Earth: the relationship between mantle, continental crust, and oceanic crust". *Earth and Planetary Science Letters* 90(3), pages 297–314. DOI: 10.1016/0012-821x(88)90132-x.

Huang, H.-H., F.-C. Lin, B. Schmandt, J. Farrell, R. B. Smith, and V. C. Tsai (2015). "The Yellowstone magmatic system from the mantle plume to the upper crust". *Science* 348(6236), pages 773–776. DOI: 10.1126/science.aaa5648.

Jambon, A., P. Lussiez, R. Clocchiatti, J. Weisz, and J. Hernandez (1992). "Olivine growth rates in a tholeiitic basalt: An experimental study of melt inclusions in plagioclase". *Chemical Geology* 96(3-4), pages 277–287. DOI: 10.1016/0009-2541(92)90059-e.

Jenner, F. E. and H. S. C. O'Neill (2012). "Major and trace analysis of basaltic glasses by laser-ablation ICP-MS". *Geochemistry, Geophysics, Geosystems* 13(3), n/a–n/a. DOI: 10.1029/2011gc003890.

Johnston, A. D. and J. R. Beckett (1986). "Compositional variation of coexisting olivine, orthopyroxene and Fe/Mg-ferrite as a function of T and f_{O_2}: a geothermometer and oxygen-barometer". *Contributions to Mineralogy and Petrology* 94(3), pages 323–332. DOI: 10.1007/bf00371441.

Johnston, A. D. and J. H. Stout (1984a). "A highly oxidized ferrian salite-, kennedyite-, forsterite-, and rhöenite-bearing alkali gabbro from Kauai, Hawaii and its mantle xenoliths". *American Mineralogist* 69(1-2), pages 57–68.

– (1984b). "Development of orthopyroxene-Fe/Mg ferrite symplectites by continuous olivine oxidation". *Contributions to Mineralogy and Petrology* 88(1-2), pages 196–202. DOI: 10.1007/bf00371423.

Johnston, A., J. H. Stout, and V. Murthy (1985). "Geochemistry and origin of some unusually oxidized alkaline rocks from Kauai, Hawaii". *Journal of Volcanology and Geothermal Research* 25(3-4), pages 225–248. DOI: 10.1016/0377-0273(85)90014-9.

Karakas, O., W. Degruyter, O. Bachmann, and J. Dufek (2017). "Lifetime and size of shallow magma bodies controlled by crustal-scale magmatism". *Nature Geoscience* 10(6), pages 446–450. DOI: 10.1038/ngeo2959.

Kohlstedt, D. L. and S. J. Mackwell (1998). "Diffusion of Hydrogen and Intrinsic Point Defects in Olivine". *Zeitschrift für Physikalische Chemie* 207(1-2), pages 147–162. DOI: 10.1524/zpch.1998.207.part_1_2.147.

Lee, C.-T. A. and E. J. Chin (2014). "Calculating melting temperatures and pressures of peridotite protoliths: Implications for the origin of cratonic mantle". *Earth and Planetary Science Letters* 403, pages 273–286. DOI: 10.1016/j.epsl.2014.06.048.

Lee, C.-T. A., P. Luffi, T. Plank, H. Dalton, and W. P. Leeman (2009). "Constraints on the depths and temperatures of basaltic magma generation on Earth and other terrestrial planets using new thermobarometers for mafic magmas".

Earth and Planetary Science Letters 279(1-2), pages 20–33. DOI: 10.1016/j.epsl.2008.12.020.

Lewis, A., M. Seckler, H. Kramer, and G. van Rosmalen (2015). *Industrial Crystallization, Fundamentals and Applications*. Cambridge University Press. ISBN: 9781107280427. DOI: 10.1017/cbo9781107280427.

Libourel, G. (1994). "Phosphorus Partitioning in Basalts: An Experimental and Ion Probe Study". *Mineralogical Magazine* 58A(2), pages 527–528. DOI: 10.1180/minmag.1994.58a.2.12.

Liu, E. J., K. V. Cashman, E. Miller, H. Moore, M. Edmonds, B. E. Kunz, F. Jenner, and G. Chigna (2020). "Petrologic monitoring at Volcán de Fuego, Guatemala". *Journal of Volcanology and Geothermal Research* 405, page 107044. DOI: 10.1016/j.jvolgeores.2020.107044.

Losantos, E., J. Cebriá, D. Morán-Zenteno, B. Martiny, J. López-Ruiz, and G. Solıs-Pichardo (2017). "Petrogenesis of the alkaline and calcalkaline monogenetic volcanism in the northern sector of the Michoacán-Guanajuato Volcanic Field (Central Mexico)". *Lithos* 288-289, pages 295–310. DOI: 10.1016/j.lithos.2017.07.013.

Lowry, R. K., P. Henderson, and J. Nolan (1982). "Tracer diffusion of some alkali, alkaline-earth and transition element ions in a basaltic and an andesitic melt, and the implications concerning melt structure". *Contributions to Mineralogy and Petrology* 80(3), pages 254–261. DOI: 10.1007/bf00371355.

Mallmann, G., H. S. C. O'Neill, and S. Klemme (2009). "Heterogeneous distribution of phosphorus in olivine from otherwise well-equilibrated spinel peridotite xenoliths and its implications for the mantle geochemistry of lithium". *Contributions to Mineralogy and Petrology* 158(4), pages 485–504. DOI: 10.1007/s00410-009-0393-6.

Milman-Barris, M. S., J. R. Beckett, M. B. Baker, A. E. Hofmann, Z. Morgan, M. R. Crowley, D. Vielzeuf, and E. Stolper (2008). "Zoning of phosphorus in igneous olivine". *Contributions to Mineralogy and Petrology* 155(6), pages 739–765. DOI: 10.1007/s00410-007-0268-7.

Mourey, A. J. and T. Shea (2019). "Forming Olivine Phenocrysts in Basalt: A 3D Characterization of Growth Rates in Laboratory Experiments". *Frontiers in Earth Science* 7. DOI: 10.3389/feart.2019.00300.

Neave, D. A., J. Maclennan, T. Thordarson, and M. E. Hartley (2015). "The evolution and storage of primitive melts in the Eastern Volcanic Zone of Iceland: the 10 ka Grımsvötn tephra series (i.e. the Saksunarvatn ash)". *Contributions to Mineralogy and Petrology* 170(2). DOI: 10.1007/s00410-015-1170-3.

Neave, D. A., O. Shorttle, M. Oeser, S. Weyer, and K. Kobayashi (2018). "Mantle-derived trace element variability in olivines and their melt inclusions". *Earth and Planetary Science Letters* 483, pages 90–104. DOI: 10.1016/j.epsl.2017.12.014.

Nicolas, A., C. Freydier, M. Godard, and A. Vauchez (1993). "Magma chambers at oceanic ridges: How large?" *Geology* 21(1), page 53. DOI: 10.1130/0091-7613(1993)021<0053:mcaorh>2.3.co;2.

Nikkola, P., G. H. Guðfinnsson, E. Bali, O. T. Rämö, T. Fusswinkel, and T. Thordarson (2019a). "Signature of deep mantle melting in South Iceland olivine". *Contributions to Mineralogy and Petrology* 174(5). DOI: 10.1007/s00410-019-1580-8.

Nikkola, P., T. Thordarson, O. T. Rämö, and P. Heikkilä (2019b). "Formation of segregation structures in Hafnarhraun pāhoehoe lobe, SW Iceland: a window into crystal–melt separation in basaltic magma". *Bulletin of Volcanology* 81(12). DOI: 10.1007/s00445-019-1330-9.

Pankhurst, M. J., D. J. Morgan, T. Thordarson, and S. C. Loughlin (2018). "Magmatic crystal records in time, space, and process, causatively linked with volcanic unrest". *Earth and Planetary Science Letters* 493, pages 231–241. DOI: 10.1016/j.epsl.2018.04.025.

Perfit, M., D. Fornari, W. Ridley, P. Kirk, J. Casey, K. Kastens, J. Reynolds, M. Edwards, D. Desonie, R. Shuster, and S. Paradis (1996). "Recent volcanism in the Siqueiros transform fault: picritic basalts and implications for MORB magma genesis". *Earth and Planetary Science Letters* 141(1-4), pages 91–108. DOI: 10.1016/0012-821x(96)00052-0.

Phelps, P. R., C.-T. A. Lee, and D. M. Morton (2020). "Episodes of fast crystal growth in pegmatites". *Nature Communications* 11(1). DOI: 10.1038/s41467-020-18806-w.

Pietruszka, A. J., D. E. Heaton, J. P. Marske, and M. O. Garcia (2015). "Two magma bodies beneath the summit of Kīlauea Volcano unveiled by isotopically distinct melt deliveries from the mantle". *Earth and Planetary Science Letters* 413, pages 90–100. DOI: 10.1016/j.epsl.2014.12.040.

Putirka, K., Y. Tao, K. Hari, M. R. Perfit, M. G. Jackson, and R. Arevalo (2018). "The mantle source of thermal plumes: Trace and minor elements in olivine and major oxides of primitive liquids (and why the olivine compositions don't matter)". *American Mineralogist* 103(8), pages 1253–1270. DOI: 10.2138/am-2018-6192.

Rae, A. S., M. Edmonds, J. Maclennan, D. Morgan, B. Houghton, M. E. Hartley, and I. Sides (2016). "Time scales of magma transport and mixing at Kīlauea Volcano, Hawai'i". *Geology* 44(6), pages 463–466. DOI: 10.1130/g37800.1.

Rasmussen, M., S. Halldórsson, S. Gibson, and G. Guðfinnsson (2020). "Olivine chemistry reveals compositional source heterogeneities within a tilted mantle plume beneath Iceland". *Earth and Planetary Science Letters* 531, page 116008. DOI: 10.1016/j.epsl.2019.116008.

Roeder, P. L. and R. F. Emslie (1970). "Olivine-liquid equilibrium". *Contributions to Mineralogy and Petrology* 29(4), pages 275–289. DOI: 10.1007/bf00371276.

Shea, T., J. E. Hammer, E. Hellebrand, A. J. Mourey, F. Costa, E. C. First, K. J. Lynn, and O. Melnik (2019). "Phosphorus and aluminum zoning in olivine: contrasting behavior of two nominally incompatible trace elements". *Contributions to Mineralogy and Petrology* 174(10). DOI: 10.1007/s00410-019-1618-y.

Simon, J. and M. Reid (2005). "The pace of rhyolite differentiation and storage in an 'archetypical' silicic magma system, Long Valley, California". *Earth and Planetary Science Letters* 235(1-2), pages 123–140. DOI: 10.1016/j.epsl.2005.03.013.

Sobolev, A. V., E. V. Asafov, A. A. Gurenko, N. T. Arndt, V. G. Batanova, M. V. Portnyagin, D. Garbe-Schönberg, and S. P. Krasheninnikov (2016). "Komatiites reveal a hydrous Archaean deep-mantle reservoir". *Nature* 531(7596), pages 628–632. DOI: 10.1038/nature17152.

Sossi, P. A. and H. S. C. O'Neill (2016). "Liquidus temperatures of komatiites and the effect of cooling rate on element partitioning between olivine and komatiitic melt". *Contributions to Mineralogy and Petrology* 171(5). DOI: 10.1007/s00410-016-1260-x.

Sunagawa, I. (2010). "Single Crystals Grown Under Unconstrained Conditions". *Springer Handbook of Crystal Growth*. Springer Berlin Heidelberg, pages 133–157. DOI: 10.1007/978-3-540-74761-1_5.

Tamura, Y., M. Yuhara, and T. Ishii (2000). "Primary Arc Basalts from Daisen Volcano, Japan: Equilibrium Crystal Fractionation versus Disequilibrium Fractionation during Supercooling". *Journal of Petrology* 41(3), pages 431–448. DOI: 10.1093/petrology/41.3.431.

Toplis, M. J. and M. R. Carroll (1996). "Differentiation of Ferro-Basaltic Magmas under Conditions Open and Closed to Oxygen: Implications for the Skaergaard Intrusion and Other Natural Systems". *Journal of Petrology* 37(4), pages 837–858. DOI: 10.1093/petrology/37.4.837.

Toplis, M. J., G. Libourel, and M. R. Carroll (1994). "The role of phosphorus in crystallisation processes of basalt: An experimental study". *Geochimica et Cosmochimica Acta* 58(2), pages 797–810. DOI: 10.1016/0016-7037(94)90506-1.

Trela, J., E. Gazel, A. V. Sobolev, L. Moore, M. Bizimis, B. Jicha, and V. G. Batanova (2017). "The hottest lavas of the Phanerozoic and the survival of deep Archaean reservoirs". *Nature Geoscience* 10(6), pages 451–456. DOI: 10.1038/ngeo2954.

Ulmer, P. (1989). "Partitioning of high field strength elements among olivine, pyroxenes, garnet and calc-alkaline picrobasalt: Experimental results and an application". *International Journal of Mass Spectrometry and Ion Physics*, pages 42–46.

Ward, K. M., G. Zandt, S. L. Beck, D. H. Christensen, and H. McFarlin (2014). "Seismic imaging of the magmatic underpinnings beneath the Altiplano-Puna volcanic complex from the joint inversion of surface wave dispersion and receiver functions". *Earth and Planetary Science Letters* 404, pages 43–53. DOI: 10.1016/j.epsl.2014.07.022.

Watkins, J. M., D. J. DePaolo, and E. B. Watson (2017). "Kinetic Fractionation of Non-Traditional Stable Isotopes by Diffusion and Crystal Growth Reactions". *Reviews in Mineralogy and Geochemistry* 82(1), pages 85–125. DOI: 10.2138/rmg.2017.82.4.

Watson, E. B. (1996). "Surface enrichment and trace-element uptake during crystal growth". *Geochimica et Cosmochimica Acta* 60(24), pages 5013–5020. DOI: 10.1016/s0016-7037(96)00299-2.

Watson, E. B., D. Cherniak, and M. Holycross (2015). "Diffusion of phosphorus in olivine and molten basalt". *American Mineralogist* 100(10), pages 2053–2065. DOI: 10.2138/am-2015-5416.

Watson, E. B. and T. Müller (2009). "Non-equilibrium isotopic and elemental fractionation during diffusion-controlled crystal growth under static and dynamic conditions". *Chemical Geology* 267(3-4), pages 111–124. DOI: 10.1016/j.chemgeo.2008.10.036.

Welsch, B., J. E. Hammer, and E. Hellebrand (2014). "Phosphorus zoning reveals dendritic architecture of olivine". *Geology* 42, pages 867–870.

Welsch, B., F. Faure, V. Famin, A. Baronnet, and P. Bachèlery (2012). "Dendritic Crystallization: A Single Process for all the Textures of Olivine in Basalts?" *Journal of Petrology* 54(3), pages 539–574. DOI: 10.1093/petrology/egs077.

Wieser, P. E., M. Edmonds, J. Maclennan, and J. Wheeler (2020). "Microstructural constraints on magmatic mushes under Kīlauea Volcano, Hawaii". *Nature Communications* 11(1). DOI: 10.1038/s41467-019-13635-y.

Workman, R. K. and S. R. Hart (2005). "Major and trace element composition of the depleted MORB mantle (DMM)". *Earth and Planetary Science Letters* 231(1-2), pages 53–72. DOI: 10.1016/j.epsl.2004.12.005.

Zamboni, D., J. Trela, E. Gazel, A. V. Sobolev, C. Cannatelli, F. Lucchi, V. G. Batanova, and B. D. Vivo (2017). "New insights into the Aeolian Islands and other arc source compositions from high-precision olivine chemistry". *Lithos* 272-273, pages 185–191. DOI: 10.1016/j.lithos.2016.12.004.

Zelenski, M., V. Kamenetsky, J. Mavrogenes, A. Gurenko, and L. Danyushevsky (2018). "Silicate-sulfide liquid immiscibility in modern arc basalt (Tolbachik volcano, Kamchatka): Part I. Occurrence and compositions of sulfide melts". *Chemical Geology* 478, pages 102–111. DOI: 10.1016/j.chemgeo.2017.09.013.

Zhang, Y., H. Ni, and Y. Chen (2010). "Diffusion Data in Silicate Melts". *Reviews in Mineralogy and Geochemistry* 72(1), pages 311–408. DOI: 10.2138/rmg.2010.72.8.

Zimmer, M. M., T. Plank, E. H. Hauri, G. M. Yogodzinski, P. Stelling, J. Larsen, B. Singer, B. Jicha, C. Mandeville, and C. J. Nye (2010). "The Role of Water in Generating the Calc-alkaline Trend: New Volatile Data for Aleutian Magmas and a New Tholeiitic Index". *Journal of Petrology* 51(12), pages 2411–2444. DOI: 10.1093/petrology/egq062.